Environ Health Perspect

DOI: 10.1289/EHP12861

Supplemental Material

Evaluation of Neural Regulation and Microglial Responses to Brain Injury in Larval Zebrafish Exposed to Perfluorooctane Sulfonate

Shannon E. Paquette, Nathan R. Martin, April Rodd, Katherine E. Manz, Eden Allen, Manuel Camarillo, Hannah I. Weller, Kurt Pennell, and Jessica S. Plavicki

Table of Contents

Table S1. Survival rate of zebrafish larvae exposed to PFOS over time.

Table S2. Primers used for qRT-PCR and genotyping.

Table S3. PFOS body burden in zebrafish larvae.

Table S4. Significantly enriched metabolic pathways following 28 µM PFOS exposure in 3 dpf larvae.

Figure S1. Microglia quantification, cell death, and proinflammatory cytokine mRNA analysis in PFOS-exposed larvae.

Figure S2. Control for the optogenetic microglia stimulation experiment by stimulating halorhodopsin negative microglia.

Figure S3. Functional neuroimaging to understand the effects of toxicant exposure on neuronal activity.

Figure S4. Regional and global brain morphology in larvae exposed to varying concentrations of PFOS.

Figure S5. MWAS of heads collected from control versus PFOS-exposed larvae.

Figure S6. Light/dark behavioral assay in larvae exposed to varying concentrations of PFOS.

Figure S7. Absolute and relative time spent in center throughout the light/dark behavioral response assay.

Figure S8. CaMPARI analysis of the habenula in larvae exposed to varying concentrations to PFOS.

Figure S9. Distance traveled in control versus PFOS-treated wildtype and macrophage mutant larvae.

Figure S10. Microglia response to brain injury in control versus PFOS-exposed versus PTZ-exposed larvae at 3 dpf.

Figure S11. Light/dark behavioral analysis in PFOA-exposed larvae.

Figure S12. Body length of 5 dpf exposed to PFOA.

References

Additional File- Excel and Video Document

Supplemental Tables

Table S1. Survival rate of zebrafish larvae exposed to PFOS over time

Age	Control	14 µM PFOS	28 µM PFOS	56 µM PFOS
24 hpf	97.93 ± 2.94	97.67 ± 1.75	98.15 ± 1.73	97.22 ± 2.84
48 hpf	97.74 ± 2.76	97.14 ± 1.21	97.09 ± 2.10	2.49 ± 2.84
72 hpf	97.43 ± 3.25	96.18 ± 1.81	95.62 ± 2.43	81.54 ± 13.23
96 hpf	96.41 ± 5.82	95.72 ± 1.20	**50.65 ± 10.06***	**25.00 ± 9.89****
120 hpf	95.93 ± 5.85	89.14 ± 3.65	**7.73 ± 3.03********	**5.33 ± 2.67********

Percent survival of larvae aged 24 hours post-fertilization (hpf) to 120 hpf following chronic exposure to control solution, 14 µM PFOS, 28 µM PFOS, or 56 µM PFOS statically starting at 4 hpf. Statistics compared each timepoint to the 24 hpf timepoint of the same treatment group using unpaired t-tests. ± denotes standard deviation. *$p < 0.05$; ***$p < 0.001$; ****$p < 0.0001$.

Table S2. Primers used for qRT-PCR and genotyping

Gene	TaqMan ID or Primer Sequences
il6 (m17)	Dr03098117_g1
il1b	Dr03114368_m1
tnfa	Dr03126850_m1
actb1 (b-actin)	Dr03432610_m1
pr2y12	F: 5’-CTTCAGGTCGTCGCTGTTTA-3’ R: 5’-AGTGCGTTTCCCTGTTGAT-3’
b-actin	F: 5’-CGAGCAGGAGATGGGAACC-3’ R: 5’-CAACGGAAACGCTCATTGC-3’
irf8	F: 5’-ACATAAGGCGTAGAGATTGGACG-3’ R: 5’- GGATGAGGACCGCACTATGTTTC-3’.

Table S3. PFOS body burden in zebrafish larvae

Chemical	Formula	MW (g/mol)	Control		28 μM PFOS		56 μM PFOS	
			48 hpf	72 hpf	48 hpf	72 hpf	48 hpf	72 hpf
PFOS	$C_8HF_{17}O_3S$	500.13	0.12 ± 0.17	0.12 ± 0.16	32.22 ± 2.57	**70.46 ± 2.72********	46.04 ± 3.75	**109.15 ± 5.99********
PFNS	$C_9HF_{19}O_3S$	550.14	0.01 ± 0.02	0.00 ± 0.00	0.19 ± 0.05	**0.39 ± 0.07********	0.23 ± 0.04	**0.69 ± 0.20*******
PFHpS	$C_7HF_{15}O_3S$	450.12	0.00 ± 0.00	0.00 ± 0.00	0.35 ± 0.17	0.45 ± 0.13	0.40 ± 0.17	**0.55 ± 0.11***
PFHxS	$C_6HF_{13}O_3S$	400.12	0.006 ± 0.01	0.008 ± 0.01	0.008 ± 0.01	0.007 ± 0.01	0.008 ± 0.01	0.008 ± 0.01

PFOS body burden (ng/embryo) in 48 hpf and 72 hpf larvae dosed with control solution, 28 μM PFOS, or 56 μM PFOS from 4 hpf. Our verification of PFOS stock solution revealed contamination by PFNS, PFHpS, and PFHxS. As such, we assessed the body burden of these compounds in the PFOS-exposed larvae, as well. Statistics compared 48 hpf to 72 hpf of the same treatment group using unpaired t-tests. ± denotes standard deviation. n = 10 pooled whole larvae from 3 experimental replicates. *$p < 0.05$; ***$p < 0.001$; ****$p < 0.0001$.

Table S4. Significantly enriched metabolic pathways following 28 µM PFOS exposure in 3 dpf larvae.

Significantly Enriched Pathway	Physiological Relevance in CNS	Source
Vitamin B1 (thiamin) metabolism	- Microglia regulation - Neuronal K^+ channels regulation - Myelinogenesis - Improves cognitive function	(1, 2)
Valine-leucine and isoleucine degradation	- Neurotransmitter metabolism, including glutamate - Protein synthesis and energy production - Nitrogen homeostasis and neurotransmitter cycling	(3, 4)
Tyrosine metabolism	- Catecholamine synthesis - Regulator of neuronal longevity	(5, 6)
Propanoate metabolism	- Modulates glutamine synthetase in glia - Inhibits histone deacetylase in GABAergic neurons, increasing GABA levels	(7, 8)
Phosphatidylinositol phosphate metabolism	- Neurotransmitter receptor expression regulation - Synaptic vesicle regulation and recycling - Neurite and dendrite morphogenesis - Clathrin-dependent membrane trafficking - Ion channel and transporter activity regulation	(9, 10)
Linoleate metabolism	- Modulates astrocyte inflammatory response - Stimulates axonal growth of cortical neurons	(11, 12)
Limonene and pinene degradation	- Represses neuronal cell death - Decreases activated glial cell number - Involved in neuroprotection - Anti-inflammatory and analgesic roles	(13)
Heparan sulfate degradation	- Regulator of axon guidance and synapse development and specificity - Involved in regulating the dopamine system - Part of the core synaptic organizing complexes neurexin and neuroligin	(14, 15)
Glyoxylate and dicarboxylate metabolism	- Important for carbohydrate metabolism and energy availability	(16)

	- Altered following traumatic brain injury	
Glutamate metabolism	- Involved in nitrogen trafficking and ammonia homeostasis in brain - Excitatory neurotransmitter and immediate precursor for the neurotransmitter GABA	(17)
Chondroitin sulfate degradation	- Role in development, plasticity, and regulation of cortical circuitry - Modulates ion channel properties - Inhibits structural plasticity (scar after injury, axonal pathfinding, and synapse formation during development) - Neuronal excitability modulation	(18)
Butanoate metabolism	- Neuromodulator largely produced by gut microbiota - Attenuates neuronal apoptosis - Inhibits amyloidogenesis - Protects neurons from ischemic damage - Improves long-term memory - Neurodegenerative attenuation	(19-21)
Aspartate and asparagine metabolism	- Secondary excitatory neurotransmission - Amino acid involved in glutamate synthesis - Influences NMDAR-mediated transmission - Can evoke presynaptic release of endogenous l-glutamate release in selective brain regions - Synaptic strength and connectivity modulation	(22, 23)

Supplemental Figures

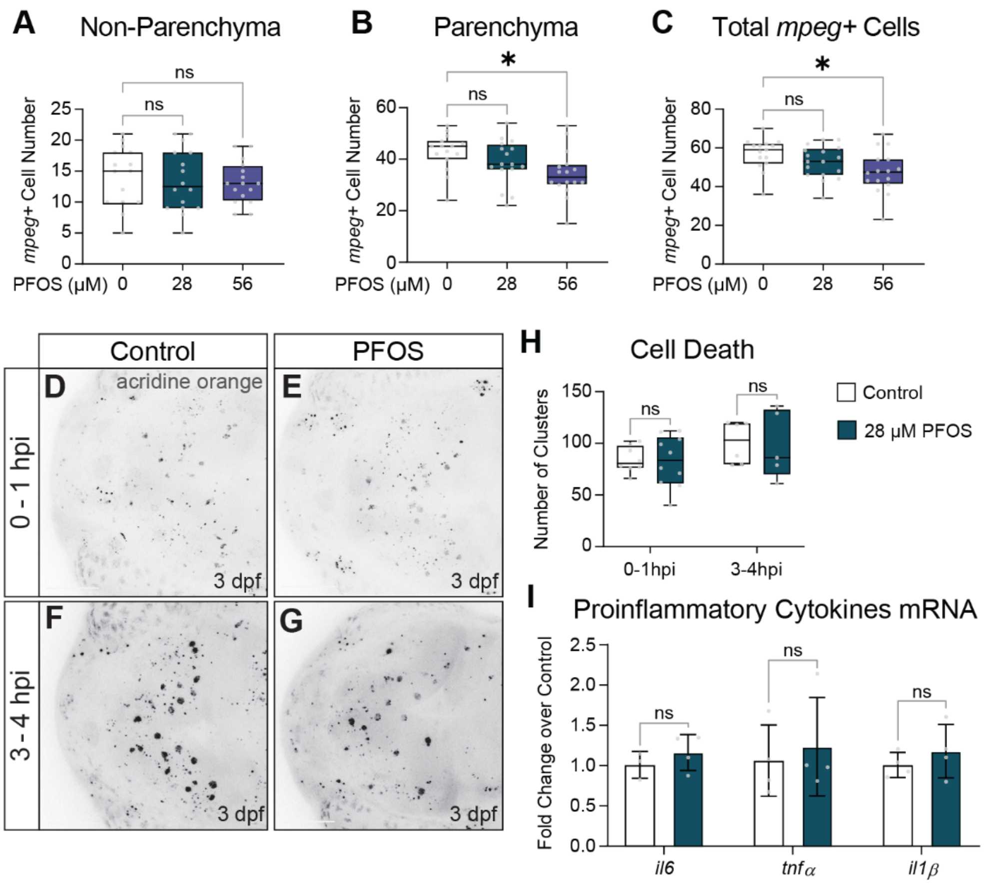

Figure S1. Microglia quantification, cell death, and proinflammatory cytokine mRNA analysis in PFOS-exposed larvae. (A) Quantification of non-parenchymal microglia at 3 days post-fertilization (dpf) in control, 28 µM, and 56 µM PFOS-exposed larvae. (B) Quantification of parenchymal microglia at 3 dpf. (C) Quantification of total microglia at 3 dpf. (D) Confocal micrograph of a 3 dpf control-treated larval brain at 1 hour post-injury (hpi) following a 1-hour live stain with 5 ug/mL acridine orange. (E) Confocal micrograph of a 3 dpf 28 µM PFOS-treated larval brain at 1 hpi following a 1-hour live stain with 5 ug/mL acridine orange. (F) Confocal micrograph of a 3 dpf control-treated larval brain at 4 hpi following a 1-hour live stain with 5 ug/mL acridine orange. (G) Confocal micrograph of a 3 dpf 28 µM PFOS-treated larval brain at 4 hpi following a 1-hour live stain with 5 ug/mL acridine orange. (H) Quantification of acridine orange positive clusters at 1 hpi and 4 hpi. n = 5-9 per group. (I) qRT-PCR results assessing the relative expression of the inflammatory genes *il6, tnfα, and il1β* in isolated heads of control- and 28 µM PFOS-treated 3 dpf larvae (n = 4 samples of 10 pooled heads). Confocal micrographs at 20x magnification. ns = not significant. **p* < 0.05. Error bars represent standard deviation. Box plot limits represent 25th to 75th percentile, with the midline representing the median. See Excel Table S1 for additional statistical details.

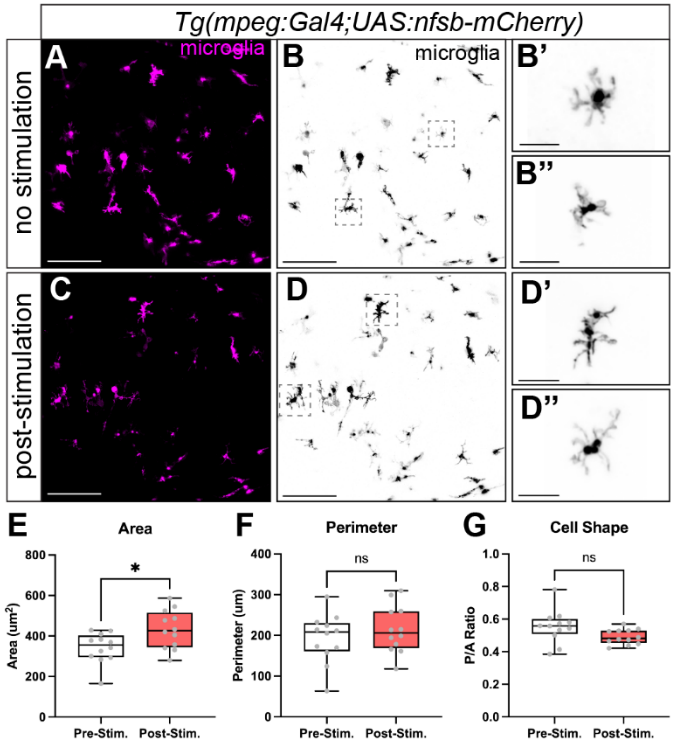

Figure S2. Control for the optogenetic microglia stimulation experiment by stimulating halorhodopsin negative microglia. (A) Confocal micrograph of a 3 dpf 28 μM-PFOS exposed brain with fluorescently-labeled microglia in magenta. Larvae were unstimulated. (B) Panel A with microglia pseudocolored in black and white. (B'-B'') 3x magnification of boxed microglia in panel B. (C) Confocal micrograph of a 3 dpf 28 μM-PFOS exposed brain with fluorescently-labeled microglia in magenta. Image taken immediately following 4-hour stimulation with 589 nm light. (D) Panel C with microglia pseudocolored in black and white. (D'-D'') 3x magnification of boxed microglia in panel D. (E) Quantification of microglia cell area with and without stimulation to 589 nm light. (F) Quantification of microglia cell perimeter with and without stimulation to 589 nm light. (G) Perimeter-to-area ratio of microglia with and without stimulation to 589 nm light. n = 12 cells per group. ns = not significant. *$p < 0.05$. Error bars represent standard deviation. Box plot limits represent 25th to 75th percentile, with the midline representing the median. See Excel Table S1 for additional statistical details.

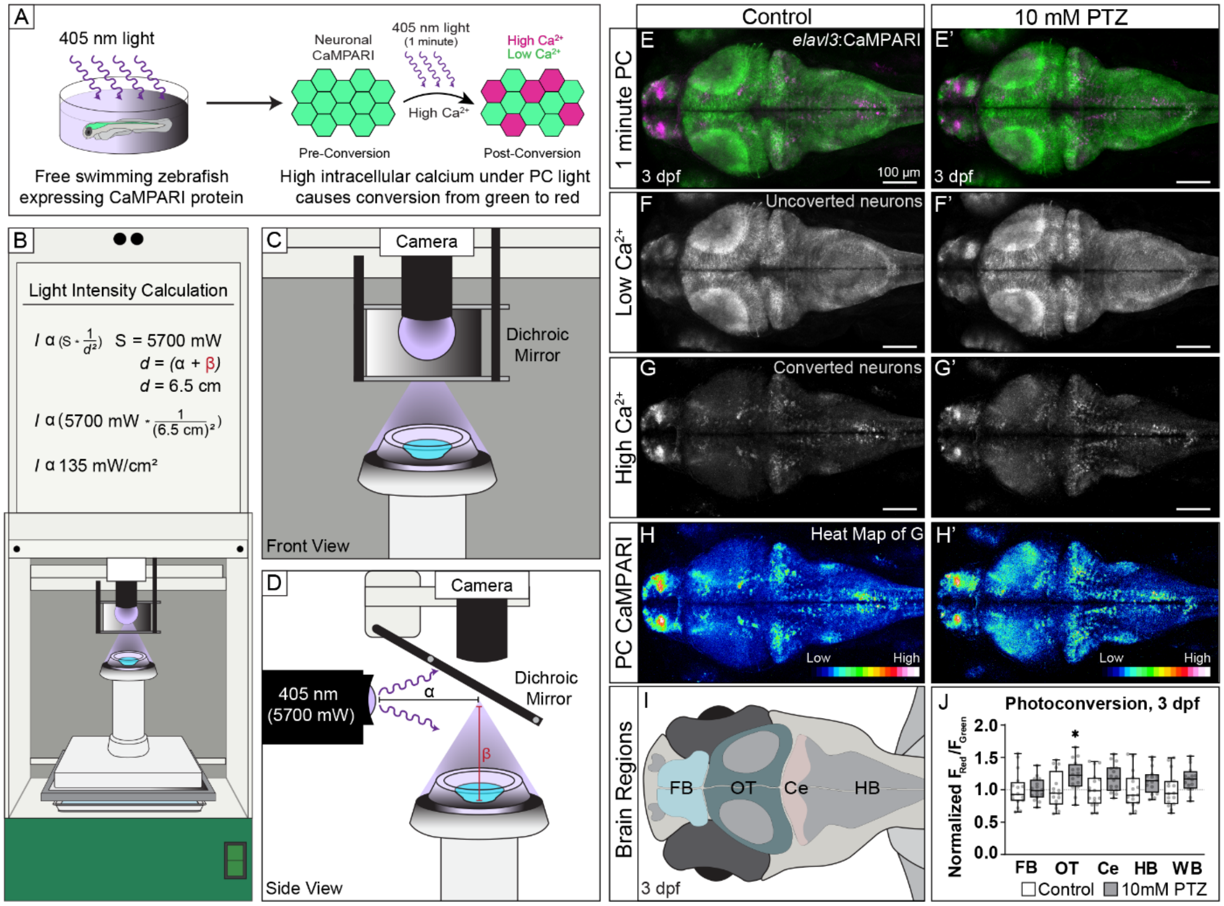

Figure S3. Functional neuroimaging to understand the effects of toxicant exposure on neuronal activity. (A) Schematic overview of CaMPARI photoconversion: free-swimming zebrafish larvae with neuron-specific expression of the genetically encoded calcium indicator CaMPARI protein (*Tg(elavl3:CaMPARI)*) are subjected to 405 nm light for 1 minute. Exposure to blue light photoconverts any neurons with high intracellular calcium from green to red. (B-D) We modified our Noldus DanioVision Behavioral unit, outfitted with LEDs for optogenetic manipulation, to efficiently photoconvert CaMPARI in free-swimming zebrafish. (B) A 3D printed pedestal was used to reduce the working distance between the light source and zebrafish larvae. Applying the inverse-square law, the light intensity at the apex of the pedestal was calculated to be 135 mW/cm². (C) Illustration of the apex of the pedestal containing a single well dish (OD 15 mm). (D) The 405 nm light had an intensity of 5700 mW at the source. The light traveled horizontally then was reflected off a dichroic mirror within the unit. The working distance was calculated as the distance from the light source to the dichroic mirror (α) plus the distance from the dichroic mirror to the apex of the pedestal (β). (E) Confocal micrographs of neuronal calcium following 1-minute photoconversion of CaMPARI in 3 dpf larvae treated with egg water or (E') after 10 minutes in 10 mM pentylenetetrazol (PTZ), a GABAA-inhibitor known to induce hyperactivity. (F, F') Green, non-active neurons with low intracellular calcium from panels E & E'. (G, G') Photoconverted, active neurons with high intracellular calcium, pseudo-labeled as magenta, from panels E & E'. (H, H') An intensity LUTs applied to the active neurons from panels G & G' spectrally mapping the regional increases of neuronal activity on a scale from less active (blue) to more active (red-white). (I) Illustrative representation of the larval zebrafish brain with labeled brain regions: forebrain (FB), optic tectum (OT), cerebellum (Ce), and hindbrain (HB). (J) Quantification of regional and global (whole brain; WB) neuronal activity by the ratio of fluorescent intensity in the red versus green channel (F_{Red}/F_{Green}). n = 16 fish per group. *$p < 0.05$. Error bars represent standard deviation. Box plot limits represent 25th to 75th percentile, with the midline representing the median. See Excel Table S1 for additional statistical details.

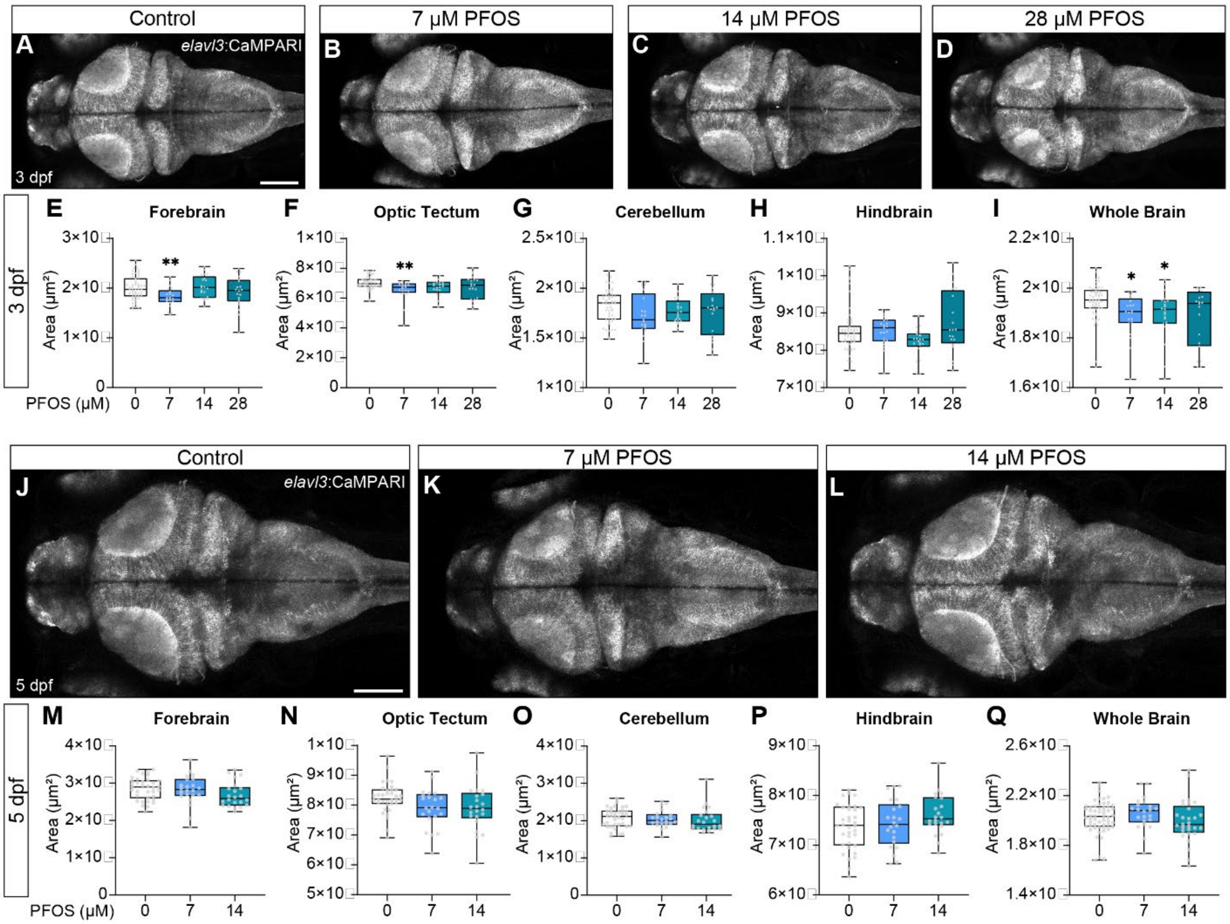

Figure S4. Regional and global brain morphology in larvae exposed to varying concentrations of PFOS. (A) Confocal micrographs of 3 dpf larvae with fluorescently labeled neurons exposed to control solution, (B) 7 μM PFOS, (C) 14 μM PFOS, or (D) 28 μM PFOS. (E) Quantification of the forebrain in 3 dpf control or PFOS-larvae. (F) Quantification of the optic tectum in 3 dpf control or PFOS-larvae. (G) Quantification of the cerebellum in 3 dpf control or PFOS-larvae. (H) Quantification of the hindbrain in 3 dpf control or PFOS-larvae. (I) Quantification of the whole brain in 3 dpf control or PFOS-larvae. (J) Confocal micrographs of 5 dpf larvae with fluorescently labeled neurons exposed to control solution, (K) 7 μM PFOS, or (L) 14 μM PFOS. (M) Quantification of the forebrain in 5 dpf control or PFOS-larvae. (N) Quantification of the optic tectum in 5 dpf control or PFOS-larvae. (O) Quantification of the cerebellum in 5 dpf control or PFOS-larvae. (P) Quantification of the hindbrain in 5 dpf control or PFOS-larvae. (Q) Quantification of the whole brain in 5 dpf control or PFOS-larvae. Confocal micrographs at 10x magnification. Control n = 52-54; treated n = 22-25. Scale bar = 100 um. *$p < 0.05$; **$p < 0.01$. Error bars represent standard deviation. Box plot limits represent 25th to 75th percentile, with the midline representing the median. See Excel Table S1 for additional statistical details.

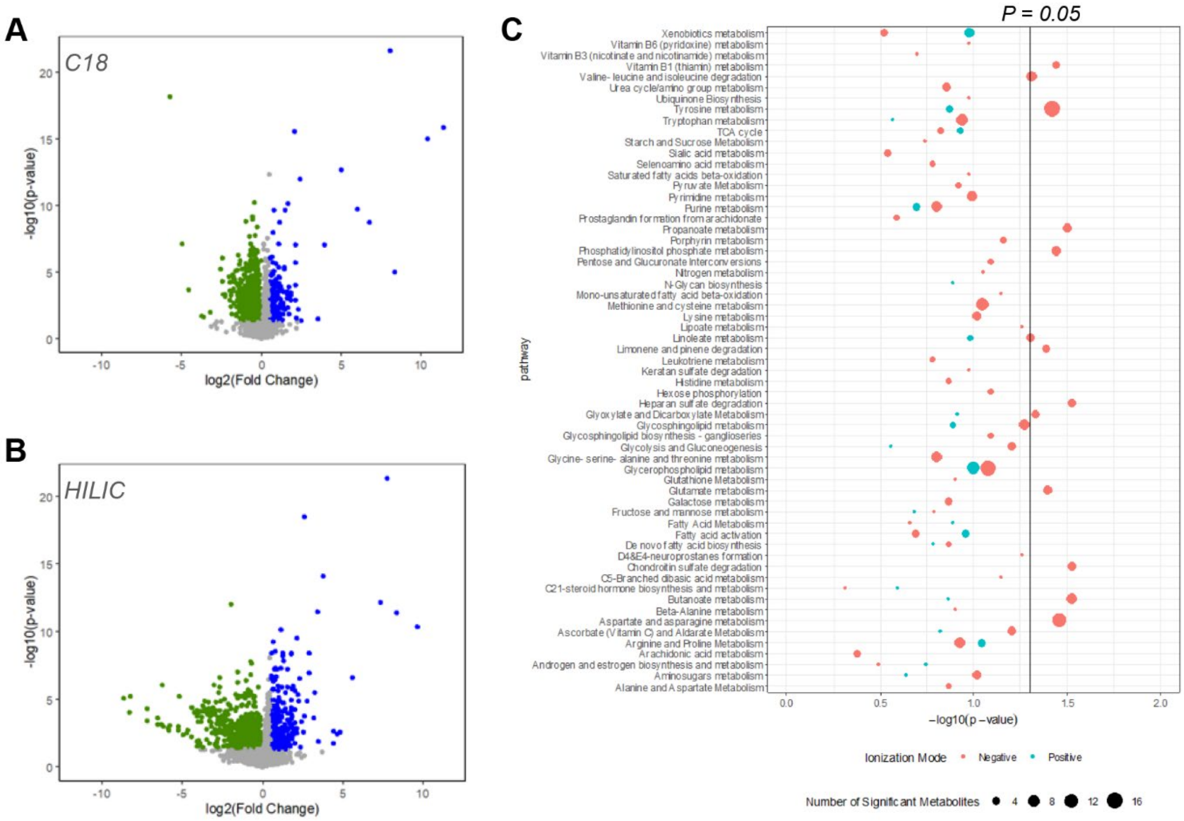

Figure S5. MWAS of heads collected from control versus PFOS-exposed larvae. Heads were collected from 3 dpf control or 28 µM PFOS exposed larvae for an untargeted metabolome wide association study (MWAS). (A) Volcano plots of metabolites detected using a C18 column with negative ionization and (B) a HILIC column with positive ionization. Green = downregulated; Blue = upregulated. Statistical significance was set at p = 0.05. (C) There are several significantly enriched pathways following both negative ionization (pink) and positive ionization (teal). The vertical line is at p = 0.05. Size of each dot represents the number of significant metabolites in that pathway. HILIC, hydrophilic interaction liquid chromatography column.

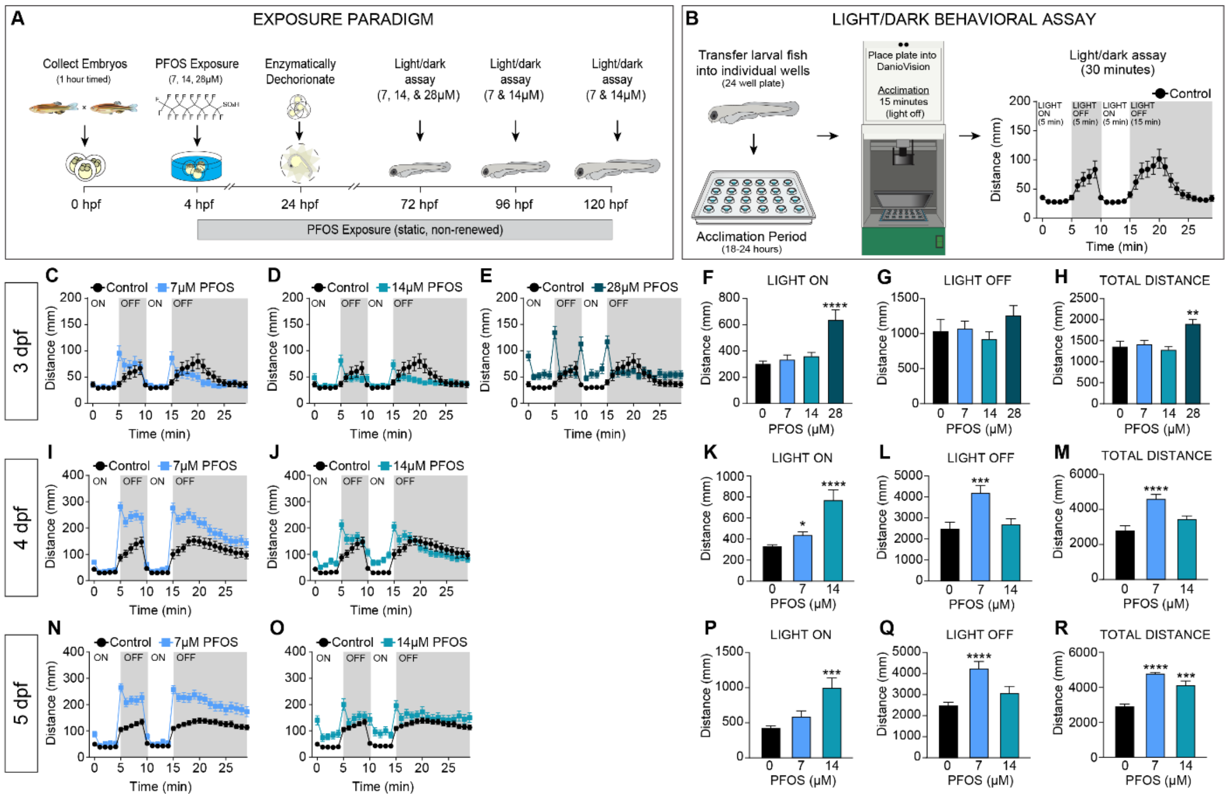

Figure S6. Light/dark behavioral assay in larvae exposed to varying concentrations of PFOS. (A) Exposure paradigm: at 4 hpf, zebrafish embryos were statically exposed to 0.1% DMSO (Control) or varying concentrations of PFOS (7, 14, or 28 μM). At 24 hpf, embryos were enzymatically dechorionated. Behavior was captured at 72, 96, and 120 hpf. (B) Light/dark behavioral assay: zebrafish larvae were placed in individual wells of a 24-well plate containing the relevant toxicant solution 18-24 hours prior to the behavior assay to allow for well acclimation. A light/dark behavioral assay was performed using the Noldus DanioVision Behavioral Unit. The light/dark behavioral assay was as follows: 15-minute acclimation in the unit with the light off, 5 minutes with the light on, 5 minutes with the light off, 5 minutes with the light on, and 15 minutes with the light off. (C) Behavioral activity plot showing distance moved (mm) over time in 3 dpf control and 7 μM PFOS-treated larvae. (D) Behavioral activity plot showing distance moved (mm) over time in 3 dpf control and 14 μM PFOS-treated larvae. (E) Behavioral activity plot showing distance moved (mm) over time in 3 dpf control and 28 μM PFOS-treated larvae. (F) Total distance moved (mm) during the light "ON" cycles in 3 dpf control and PFOS-treated larvae. (G) Total distance moved (mm) during the light "OFF" cycles in 3 dpf control and PFOS-treated larvae. (H) Total distance moved (mm) during the entire behavior assay in 3 dpf control and PFOS-treated larvae. (I) Behavioral activity plot showing distance moved (mm) over time in 4 dpf control and 7 μM PFOS-treated larvae. (J) Behavioral activity plot showing distance moved (mm) over time in 4 dpf control and 14 μM PFOS-treated larvae. (K) Total distance moved (mm) during the light "ON" cycles in 4 dpf control and PFOS-treated larvae. (L) Total distance moved (mm) during the light "OFF" cycles in 4 dpf control and PFOS-treated larvae. (M) Total distance moved (mm) during the entire behavior assay in 4 dpf control and PFOS-treated larvae. (N) Behavioral activity plot showing distance moved (mm) over time in 5 dpf control and 7 μM PFOS-treated larvae. (O) Behavioral activity plot showing distance moved (mm) over time in 5 dpf control and 14 μM PFOS-treated larvae. (P) Total distance moved (mm) during the light "ON" cycles in 5 dpf control and PFOS-treated larvae. (Q) Total distance moved (mm) during the light "OFF" cycles in 5 dpf control and PFOS-treated larvae. (R) Total distance moved (mm) during the entire behavior assay in 5 dpf control and PFOS-treated larvae. Control n = 130-190, treated n

= 88-99. *p < 0.05; **p < 0.01; ***p < 0.001; ****p < 0.0001. Error bars represent SEM. See Excel Table S1 for additional statistical details.

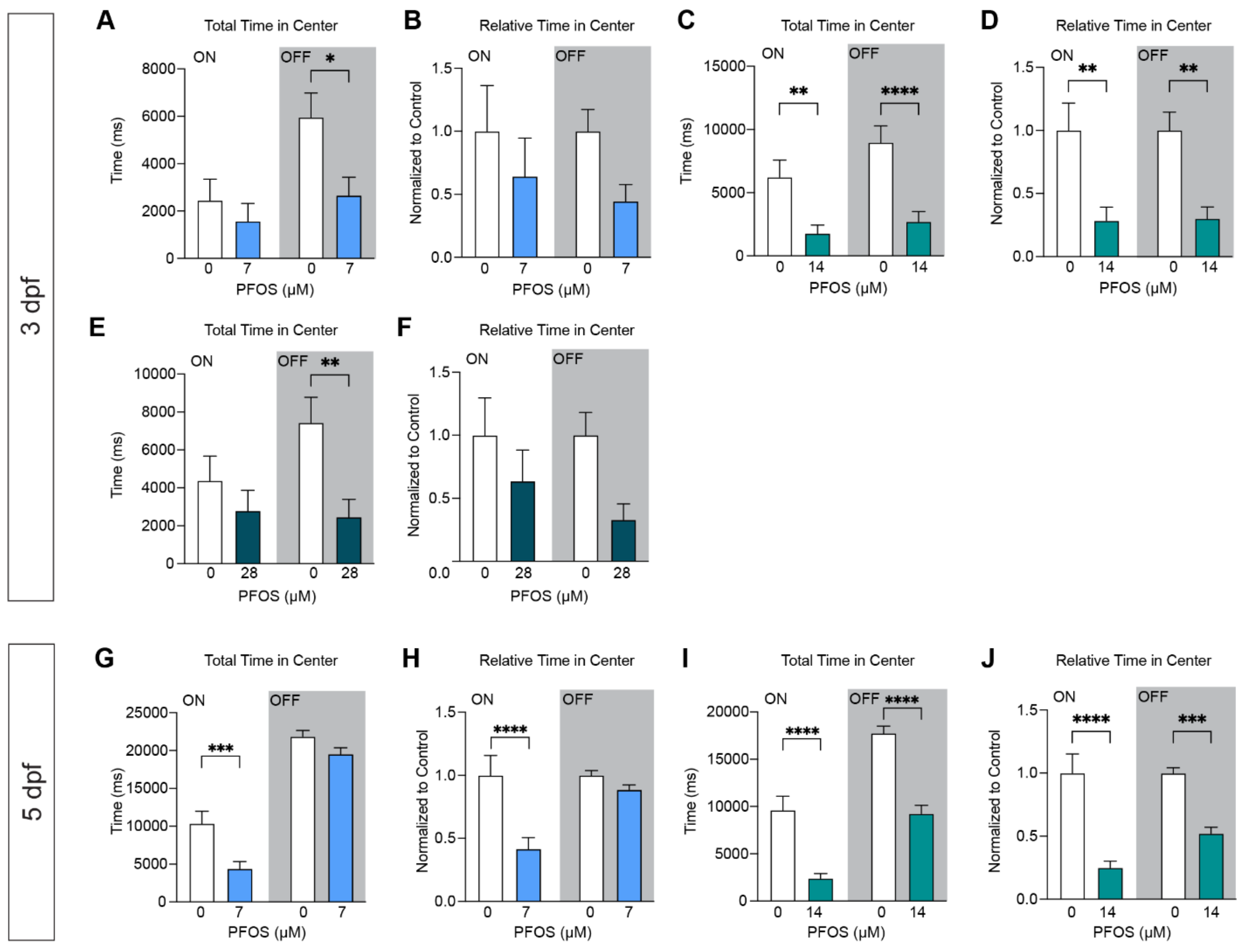

Figure S7. Absolute and relative time spent in center throughout the light/dark behavioral response assay. (A) Total time spent in the center of the well during the light on and light off cycles in 3 dpf control and 7 µM PFOS-treated larvae. (B) Relative time spent in the center during the light on and light off cycles in 3 dpf control and 7 µM PFOS-treated larvae. (C) Total time spent in the center during the light on and light off cycles in 3 dpf control and 14 µM PFOS-treated larvae. (D) Relative time spent in the center during the light on and light off cycles in 3 dpf control and 14 µM PFOS-treated larvae. (E) Total time spent in the center during the light on and light off cycles in 3 dpf control and 28 µM PFOS-treated larvae. (F) Relative time spent in the center during the light on and light off cycles in 3 dpf control and 28 µM PFOS-treated larvae. (G) Total time spent in the center during the light on and light off cycles in 5 dpf control and 7 µM PFOS-treated larvae. (H) Relative time spent in the center during the light on and light off cycles in 5 dpf control and 7 µM PFOS-treated larvae. (I) Total time spent in the center during the light on and light off cycles in 5 dpf control and 14 µM PFOS-treated larvae. (J) Relative time spent in the center during the light on and light off cycles in 5 dpf control and 14 µM PFOS-treated larvae. Control n = 88-102; treated n = 84-

100. *$p < 0.05$; **$p < 0.01$; ***$p < 0.001$; ****$p < 0.0001$. Error bars represent SEM. See Excel Table S1 for additional statistical details.

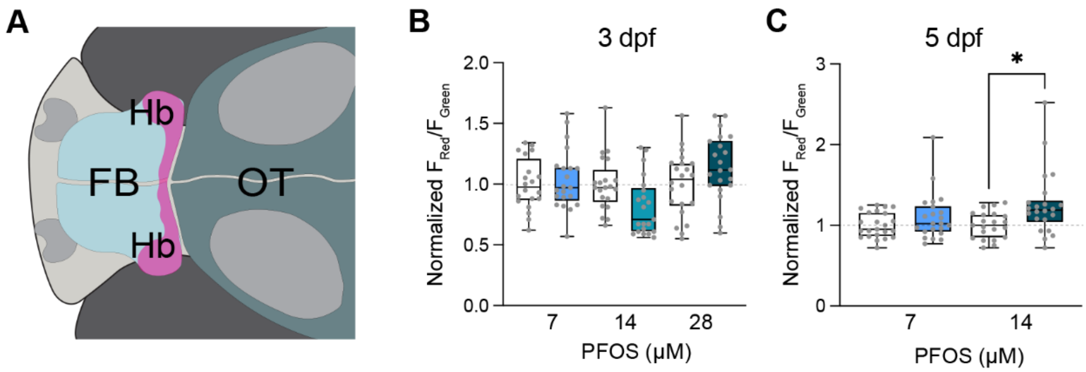

Figure S8. CaMPARI analysis of the habenula in larvae exposed to varying concentrations to PFOS. (A) Illustrative representation of a larval zebrafish brain with anatomical regions outlined: forebrain (FB), habenula (Hb), and optic tectum (OT). Activity quantification of neuron-driven CaMPARI was performed in the entire developing habenula following 1-minute exposure to 405 nm light at (B) 3 dpf and (C) 5 dpf in control or PFOS-treated larvae. n = 20-22 fish per treatment. *$p < 0.05$. Error bars represent standard deviation. Box plot limits represent 25^{th} to 75^{th} percentile, with the midline representing the median. See Excel Table S1 for additional statistical details.

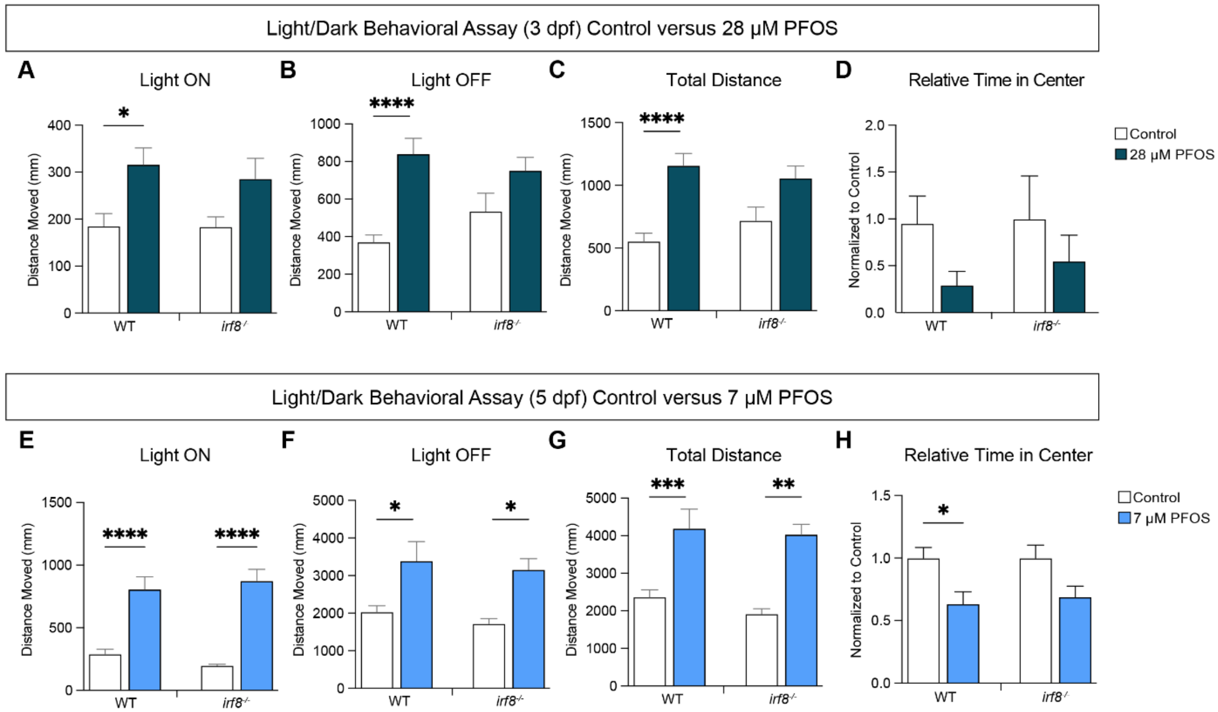

Figure S9. Distance traveled in control versus PFOS-treated wildtype and macrophage mutant larvae. (A) Distance moved (mm) in 3 dpf control or PFOS-treated wildtype (WT) and *irf8*$^{-/-}$ mutant larvae during the light "ON" cycles, (B) light "OFF" cycles, and (C) throughout the whole behavioral assay. (D) Relative time 3 dpf PFOS-treated WT and *irf8*$^{-/-}$ mutant larvae spent in the center of the well compared to control-treated WT larvae. (E) Distance moved (mm) in 5 dpf control or PFOS-treated WT and *irf8*$^{-/-}$ mutant larvae during the light "ON" cycles, (F) light "OFF" cycles, and (G) throughout the whole behavioral assay. (H) Relative time 5 dpf PFOS-treated WT and *irf8*$^{-/-}$ mutant larvae spent in the center of the well compared to control-treated WT larvae. n = 14-22 per group. *$p < 0.05$; **$p < 0.01$; ***$p < 0.001$; ****$p < 0.0001$. Error bars represent SEM. See Excel Table S1 for additional statistical details.

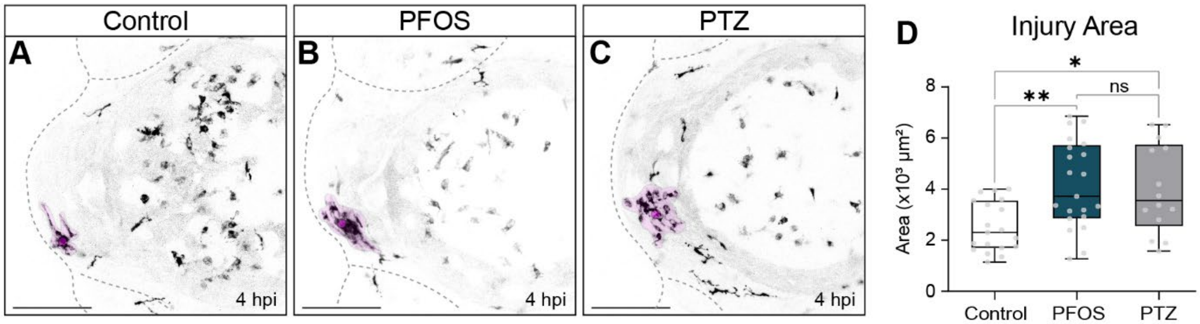

Figure S10. Microglia response to brain injury in control versus PFOS-exposed versus PTZ-exposed larvae at 3 dpf. Larvae with transgenic expression of macrophages (Tg(*mpeg1:EGFP*)) were dosed with either (A) control or (B) 28 µM PFOS at 4 hpf, or (C) 5 mM PTZ at 72 hpf, followed by brain injury. Confocal micrographs are representative images at 4 hpi, with the area of microglia response shaded in the magenta. (D) Quantification of the area of responding microglia around the injury site at 4 hpi. n = 14-21 per group. ns = not significant. *$p < 0.05$; **$p < 0.01$. Error bars represent standard deviation. Box plot limits represent 25th to 75th percentile, with the midline representing the median. See Excel Table S1 for additional statistical details.

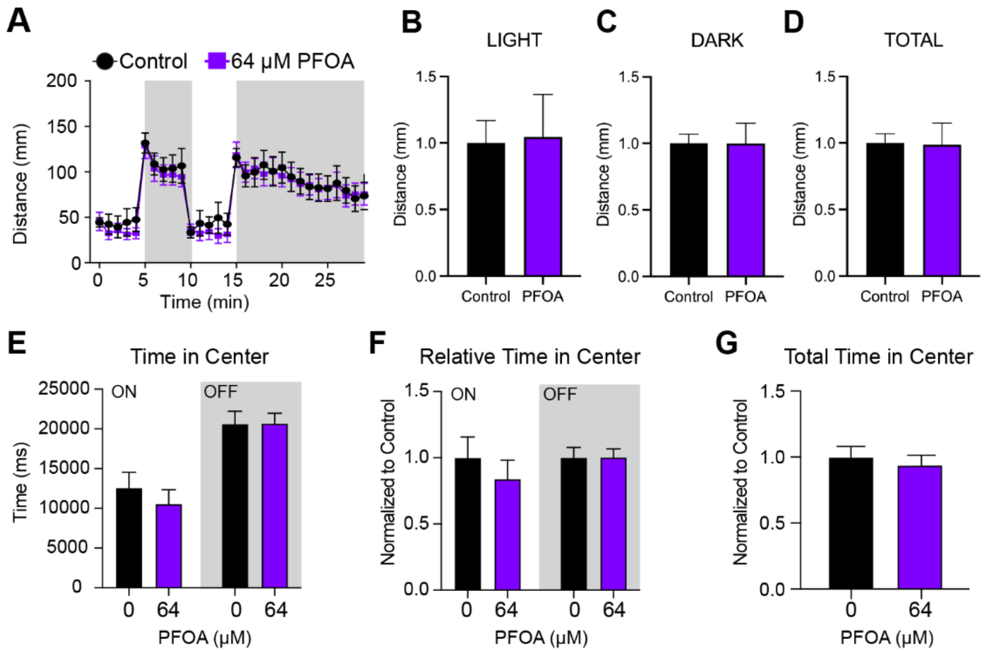

Figure S11. Light/dark behavioral analysis in PFOA-exposed larvae. Zebrafish larvae were subjected to a 30-minute light/dark behavioral assay at 5 dpf. (A) Behavioral activity plot of distance moved (mm) over time in 5 dpf control or 64 μM PFOA-treated larvae. (B) Distance moved during the light "ON" cycles in PFOA-treated larvae relative to controls. (C) Distance moved during the light "OFF" cycles in PFOA-treated larvae relative to controls. (D) Total distance moved throughout the behavioral assay in PFOA-treated larvae relative to controls. (E) Time (ms) 5 dpf control or 64 μM PFOA-treated larvae spent in the center of the well during the light "ON" and light "OFF" cycles. (F) Relative time 5 dpf 64 μM PFOA-treated larvae spent in the center of the well during the light "ON" and light "OFF" cycles relative to controls. (G) Total time 5 dpf 64 μM PFOA-treated larvae spent in the center of the well relative to controls. n = 24 control and n = 46 treated for behavior analyses; n = 37 control and n = 35 treated for anxiety analyses. Error bars represent SEM. See Excel Table S1 for additional statistical details.

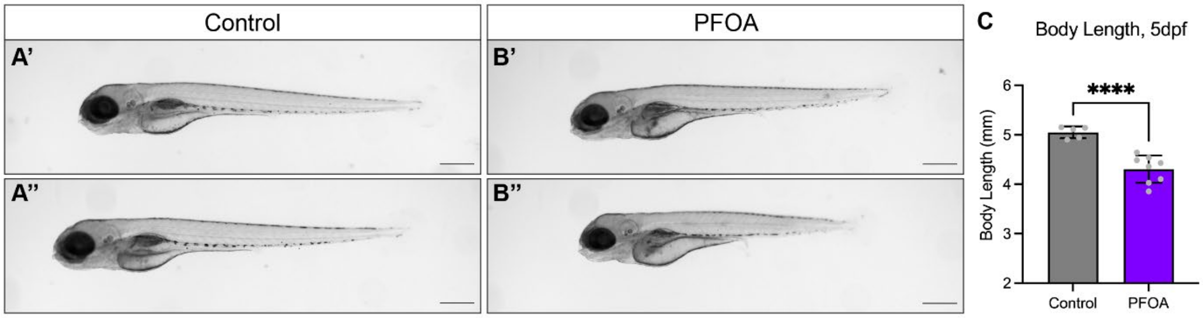

Figure S12. Body length of 5 dpf exposed to PFOA. (A'-A'') Images of 5 dpf control-treated larvae. (B'-B'') Images of 5 dpf larvae statically treated with 64 μM PFOA. (C) Body length measurements of control versus PFOA treatment at 5 dpf. ****p < 0.0001. n = 5-8 per group. Scale = 500 um. Error bars represent standard deviation. See Excel Table S1 for additional statistical details.

References

1. Ba A. Metabolic and structural role of thiamine in nervous tissues. Cell Mol Neurobiol. 2008 Nov;28(7):923-31. Epub 20080719. doi:10.1007/s10571-008-9297-7. Cited in: Pubmed; PMID 18642074.

2. Mkrtchyan G, Aleshin V, Parkhomenko Y, Kaehne T, Di Salvo ML, Parroni A, Contestabile R, Vovk A, Bettendorff L, Bunik V. Molecular mechanisms of the non-coenzyme action of thiamin in brain: biochemical, structural and pathway analysis. Sci Rep. 2015 Jul 27;5:12583. Epub 20150727. doi:10.1038/srep12583. Cited in: Pubmed; PMID 26212886.

3. Polis B, Samson AO. Role of the metabolism of branched-chain amino acids in the development of Alzheimer's disease and other metabolic disorders. Neural Regen Res. 2020 Aug;15(8):1460-1470. None. doi:10.4103/1673-5374.274328. Cited in: Pubmed; PMID 31997805.

4. Salcedo C, Andersen JV, Vinten KT, Pinborg LH, Waagepetersen HS, Freude KK, Aldana BI. Functional Metabolic Mapping Reveals Highly Active Branched-Chain Amino Acid Metabolism in Human Astrocytes, Which Is Impaired in iPSC-Derived Astrocytes in Alzheimer's Disease. Front Aging Neurosci. 2021;13:736580. The authors declare that the research was conducted in the absence of any commercial or financial relationships that could be construed as a potential conflict of interest. Epub 20210917. doi:10.3389/fnagi.2021.736580. Cited in: Pubmed; PMID 34603012.

5. Kobayashi K, Morita S, Sawada H, Mizuguchi T, Yamada K, Nagatsu I, Hata T, Watanabe Y, Fujita K, Nagatsu T. Targeted disruption of the tyrosine hydroxylase locus results in severe catecholamine depletion and perinatal lethality in mice. J Biol Chem. 1995 Nov 10;270(45):27235-43. Epub 1995/11/10. doi:10.1074/jbc.270.45.27235. Cited in: Pubmed; PMID 7592982.

6. Parkhitko AA, Ramesh D, Wang L, Leshchiner D, Filine E, Binari R, Olsen AL, Asara JM, Cracan V, Rabinowitz JD, Brockmann A, Perrimon N. Downregulation of the tyrosine degradation pathway extends Drosophila lifespan. Elife. 2020 Dec 15;9. AP, DR, LW, DL, EF, RB, AO, JA, VC, JR, AB, NP No competing interests declared. Epub 20201215. doi:10.7554/eLife.58053. Cited in: Pubmed; PMID 33319750.

7. Morland C, Froland AS, Pettersen MN, Storm-Mathisen J, Gundersen V, Rise F, Hassel B. Propionate enters GABAergic neurons, inhibits GABA transaminase, causes GABA accumulation and lethargy in a model of propionic acidemia. Biochem J. 2018 Feb 16;475(4):749-758. Epub 20180216. doi:10.1042/BCJ20170814. Cited in: Pubmed; PMID 29339464.

8. Nguyen NH, Morland C, Gonzalez SV, Rise F, Storm-Mathisen J, Gundersen V, Hassel B. Propionate increases neuronal histone acetylation, but is metabolized oxidatively by glia.

Relevance for propionic acidemia. J Neurochem. 2007 May;101(3):806-14. Epub 20070205. doi:10.1111/j.1471-4159.2006.04397.x. Cited in: Pubmed; PMID 17286595.

9. Clayton EL, Minogue S, Waugh MG. Phosphatidylinositol 4-kinases and PI4P metabolism in the nervous system: roles in psychiatric and neurological diseases. Mol Neurobiol. 2013 Feb;47(1):361-72. Epub 20121010. doi:10.1007/s12035-012-8358-6. Cited in: Pubmed; PMID 23054682.

10. Raghu P, Joseph A, Krishnan H, Singh P, Saha S. Phosphoinositides: Regulators of Nervous System Function in Health and Disease. Front Mol Neurosci. 2019;12:208. Epub 2019/09/12. doi:10.3389/fnmol.2019.00208. Cited in: Pubmed; PMID 31507376.

11. Saba F, Sirigu A, Pillai R, Caria P, Cordeddu L, Carta G, Murru E, Sogos V, Banni S. Downregulation of inflammatory markers by conjugated linoleic acid isomers in human cultured astrocytes. Nutr Neurosci. 2019 Mar;22(3):207-214. Epub 20170829. doi:10.1080/1028415X.2017.1367130. Cited in: Pubmed; PMID 28847225.

12. Hennebelle M, Morgan RK, Sethi S, Zhang Z, Chen H, Grodzki AC, Lein PJ, Taha AY. Linoleic acid-derived metabolites constitute the majority of oxylipins in the rat pup brain and stimulate axonal growth in primary rat cortical neuron-glia co-cultures in a sex-dependent manner. J Neurochem. 2020 Jan;152(2):195-207. Epub 20191126. doi:10.1111/jnc.14818. Cited in: Pubmed; PMID 31283837.

13. Eddin LB, Jha NK, Meeran MFN, Kesari KK, Beiram R, Ojha S. Neuroprotective Potential of Limonene and Limonene Containing Natural Products. Molecules. 2021 Jul 27;26(15). Epub 20210727. doi:10.3390/molecules26154535. Cited in: Pubmed; PMID 34361686.

14. Condomitti G, de Wit J. Heparan Sulfate Proteoglycans as Emerging Players in Synaptic Specificity. Front Mol Neurosci. 2018;11:14. Epub 20180126. doi:10.3389/fnmol.2018.00014. Cited in: Pubmed; PMID 29434536.

15. De Risi M, Tufano M, Alvino FG, Ferraro MG, Torromino G, Gigante Y, Monfregola J, Marrocco E, Pulcrano S, Tunisi L, Lubrano C, Papy-Garcia D, Tuchman Y, Salleo A, Santoro F, Bellenchi GC, Cristino L, Ballabio A, Fraldi A, De Leonibus E. Altered heparan sulfate metabolism during development triggers dopamine-dependent autistic-behaviours in models of lysosomal storage disorders. Nat Commun. 2021 Jun 9;12(1):3495. Epub 20210609. doi:10.1038/s41467-021-23903-5. Cited in: Pubmed; PMID 34108486.

16. Baker EW, Henderson WM, Kinder HA, Hutcheson JM, Platt SR, West FD. Scaled traumatic brain injury results in unique metabolomic signatures between gray matter, white matter, and serum in a piglet model. PLoS One. 2018;13(10):e0206481. The authors have declared that no competing interests exist. Epub 20181031. doi:10.1371/journal.pone.0206481. Cited in: Pubmed; PMID 30379914.

17. Schousboe A, Scafidi S, Bak LK, Waagepetersen HS, McKenna MC. Glutamate metabolism in the brain focusing on astrocytes. Adv Neurobiol. 2014;11:13-30. doi:10.1007/978-3-319-08894-5_2. Cited in: Pubmed; PMID 25236722.

18. Hudson AE, Gollnick C, Gourdine JP, Prinz AA. Degradation of extracellular chondroitin sulfate delays recovery of network activity after perturbation. J Neurophysiol. 2015 Aug;114(2):1346-52. Epub 20150624. doi:10.1152/jn.00455.2015. Cited in: Pubmed; PMID 26108956.

19. Kim SY, Chae CW, Lee HJ, Jung YH, Choi GE, Kim JS, Lim JR, Lee JE, Cho JH, Park H, Park C, Han HJ. Sodium butyrate inhibits high cholesterol-induced neuronal amyloidogenesis by modulating NRF2 stabilization-mediated ROS levels: involvement of NOX2 and SOD1. Cell Death Dis. 2020 Jun 18;11(6):469. Epub 20200618. doi:10.1038/s41419-020-2663-1. Cited in: Pubmed; PMID 32555166.

20. Xu Y, Peng S, Cao X, Qian S, Shen S, Luo J, Zhang X, Sun H, Shen WL, Jia W, Ye J. High doses of butyrate induce a reversible body temperature drop through transient proton leak in mitochondria of brain neurons. Life Sci. 2021 Aug 1;278:119614. Epub 20210519. doi:10.1016/j.lfs.2021.119614. Cited in: Pubmed; PMID 34022200.

21. Zhou Z, Xu N, Matei N, McBride DW, Ding Y, Liang H, Tang J, Zhang JH. Sodium butyrate attenuated neuronal apoptosis via GPR41/Gbetagamma/PI3K/Akt pathway after MCAO in rats. J Cereb Blood Flow Metab. 2021 Feb;41(2):267-281. Epub 20200309. doi:10.1177/0271678X20910533. Cited in: Pubmed; PMID 32151222.

22. Pardo B, Rodrigues TB, Contreras L, Garzon M, Llorente-Folch I, Kobayashi K, Saheki T, Cerdan S, Satrustegui J. Brain glutamine synthesis requires neuronal-born aspartate as amino donor for glial glutamate formation. J Cereb Blood Flow Metab. 2011 Jan;31(1):90-101. Epub 20100825. doi:10.1038/jcbfm.2010.146. Cited in: Pubmed; PMID 20736955.

23. Errico F, Nuzzo T, Carella M, Bertolino A, Usiello A. The Emerging Role of Altered d-Aspartate Metabolism in Schizophrenia: New Insights From Preclinical Models and Human Studies. Front Psychiatry. 2018;9:559. Epub 20181106. doi:10.3389/fpsyt.2018.00559. Cited in: Pubmed; PMID 30459655.